nature portfolio

https://doi.org/10.1038/s41550-021-01569-9

Supplementary information

Burst timescales and luminosities as links between young pulsars and fast radio bursts

In the format provided by the authors and unedited

Supplementary Information

Fluence and luminosity

The burst profiles, in S/N units, are converted to physical units (flux density, Jy) using the radiometer equation[80], using typical values for Effelsberg's 1.4 GHz receiver temperature (20 K) and gain (1.54 Jy K^{-1}). We expect these system values to be accurate to within 20%, which dominates the errors on the peak flux density and fluence (note that the peak flux density depends strongly on the time resolution used, and the values reported in Table 1 are calculated using a time resolution of 8 μs). We additionally consider a sky background temperature of 0.8 K, by extrapolating from the 408 MHz map[81], using a spectral index of −2.7[82], and adding a 3 K contribution from the cosmic microwave background[83]. For the 8 μs burst profiles, we report the peak S/N, peak flux density and fluence (measured in the $\pm 2\sigma$ width region) in Table 1. We also report the isotropic-equivalent spectral luminosity of the bursts, taking the distance to FRB 20200120E as 3.63 ± 0.34 Mpc[22].

Burst temporal extent and spectral structure

We performed a 2-dimensional Gaussian fit to the burst dynamic spectra (Figure 2), to determine the burst extents in time and frequency. The measured widths were clearly underestimated compared with what can be seen by eye in the dynamic spectra, likely since the bursts are not well-modelled by a 2-dimensional Gaussian function. In the case of B1, B3, B4, and B5 we use the Gaussian mean in time as the Time=0 reference in Figure 2, and use this to calculate the burst time of arrival corrected to the Solar System Barycenter at infinite frequency, reported in Table 1. For B2, since there are two clear burst components, we fit a 2-dimensional Gaussian to each and determined the Time=0 reference as the center of the means of those Gaussians. Note that we do not fit pulse broadening functions to estimate the scattering timescale since the estimated scattering timescale from the Milky Way ISM is ∼ 50 ns (≪ 8 μs) at 1.4 GHz[29], and is consistent with the frequency structure we attribute to scintillation (see below).

To more accurately determine the burst widths, we performed a 2-dimensional autocorrelation of the dynamic spectra, and fit these with 2-dimensional Gaussian functions (Extended Data Figure 2). Note the zero-lag noise spike is removed from this ACF. We convert the standard deviation of this Gaussian fit (in both time and frequency) to a full-width at half-maximum (FWHM) by multiplying the standard deviation by the factor $2\sqrt{2\ln(2)}$. We report the burst time width ($t_{wid} = 1/\sqrt{2} \times$ FWHM) and frequency extent (ν_{wid} = FWHM) in Table 1. In Figure 2, the colored bars below each burst profile indicate the $\pm 2\sigma$ width used for calculations of the fluence and polarization fractions.

In addition to the frequency extent measured with the 2-dimensional ACF, there is another, narrower frequency scale evident in the one-dimensional frequency ACF (or simply by eye in the dynamic spectra of the bright bursts). Shown in Extended Data Figure 3a is the frequency ACF after subtracting the larger frequency scale Gaussian. We perform a least-squares fit of a Lorentzian function to the center of this ACF (defined by eye using the clearly visible central feature in the ACF; Extended Data Figure 3a). A Lorentzian frequency ACF is expected for scintillation[84]. The fit function is of the form

$$\frac{a}{x^2 + \nu_{\rm scale}^2} + b, \tag{5}$$

where a is the amplitude, b is a vertical offset, and $\nu_{\rm scale}$ is the scintillation bandwidth (defined as the half-width at half-maximum of the ACF[84]). The scintillation bandwidth measurements are reported in Table 1. The Galactic ISM is expected to introduce a broadening due to scattering of ∼ 50 ns (at 1.4 GHz) along this line-of-sight[29], in rough agreement with our measured scintillation bandwidth ($1/(2\pi\Delta\nu_{\rm scint}) \sim 27$ ns). We therefore attribute this narrower spectral structure to scintillation from the Milky Way ISM. This interpretation is supported by the stronger correlation in the spectrum of two bursts (B1 and B2) separated by 4.3 minutes, compared to the lack of correlation between bursts B3 and B4, which are separated by 2.5 hrs (Supplementary Figure 2). The expected scintillation time is ∼ 10 minutes (at 1.4 GHz) at high Galactic latitudes, which is dependent on an effective velocity (the assumption for Galactic sources is 100 km s^{-1})[29,85]. This effective velocity is likely smaller for an extragalactic source than for a Galactic pulsar in the same line of sight, since the effective velocity is usually dominated by the velocity of the pulsar. Assuming an effective velocity of ∼ 30 km s^{-1}, the expected scintillation time will be ∼ 30 minutes (at 1.4 GHz), consistent with the decorrelation timescale constraints using FRB 20200120E.

Polarization calibration

To study the polarization properties of the bursts, we must first calibrate the data. In these observations, we did not record a noise diode scan to use for delay calibration; instead, we use the test pulsar data, also taken to inspect the general data quality, to calibrate the polarimetric data. This analysis strategy has been used successfully in previous work to determine the polarimetric properties of radio bursts from the Galactic magnetar SGR 1935+2154, detected using voltage data of the Westerbork RT1 VLBI backend[42], and also in a study of the repeating FRB 20180916B, using data from the Effelsberg telescope as part of an EVN campaign[15]. Since we detected bursts on separate epochs, we calibrate the data using the test pulsar scan closest in time to the bursts. B1 and B2 are < 1 hr from the PSR B0355+54 calibration scan, and B3 and B4 are ∼ 4 hr and < 2 hr from the PSR B0355+54 scan, respectively. We note that we could not recover the polarimetric properties of burst B5 likely due to the low S/N of the burst, and so the April 28 epoch is omitted from the remainder of this section.

The data could exhibit leakage between the polarization channels, which we assume only significantly affects Stokes V (defined as V=LL−RR using the PSR/IEEE convention[86]). In the pulsar data, without calibrating the leakage, we reproduce the circular polarization fraction to within 3% and 1% of the published values[87], for the Feb 20 and Mar 7 epochs, respectively. We, therefore, apply no leakage calibration.

A delay between the polarization hands is more crucial to correct for since it can significantly impact our interpretation of the linear polarization fraction and RM. Using the known RM of PSR B0355+54, 79 rad m^{-2} [30], we performed a brute-force search for the delay between polarization hands, D, that maximises the linear polarization, by rotating the data using the factor

$$e^{-2i\mathrm{RM}(c^2/\nu^2)}e^{-2i\nu\pi D}, \quad (6)$$

where c is the speed of light and ν is the frequency in Hz. We searched for delays between −15 and 15 ns, in steps of 0.01 ns. Note that previous work with the VLBI recorder at Effelsberg showed an instrumental delay of 5.4 ns [15]. The estimated delays are −0.18 ns and −4.11 ns for the Feb 20 and Mar 7 observations, respectively.

After removing the effect of the estimated delays, we performed RM synthesis [88] on the burst data to estimate the RMs of the bursts. The Faraday spectra for each burst are shown in Supplementary Figure 3a.

To refine the RM and delay measurements further, we performed a joint least squares fit of Stokes Q and U spectra normalised by the linear polarization L= $\sqrt{\mathrm{Q}^2 + \mathrm{U}^2}$, using the following equations

$$Q/L = \cos(2(c^2\mathrm{RM}/\nu^2 + \nu\pi D + \phi)), \quad (7)$$

$$U/L = \sin(2(c^2\mathrm{RM}/\nu^2 + \nu\pi D + \phi)), \quad (8)$$

where ϕ is a linear combination of the absolute angle of polarisation on the sky (referenced to infinite frequency) and the phase difference between the R and L polarisation channels. The estimates of the delay and RM are given as initial guesses to the fit, and we simultaneously fit the pulsar and the two bursts from the same observational epoch. We force the delay to be the same between the pulsar and FRB data, fix to the known RM of the pulsar (79 rad m^{-2}), and initially we allow for a different RM per burst. The measured delays are -0.22 ± 0.02 ns and -4.16 ± 0.03 ns, for the Feb 20 and Mar 7 observations, respectively, and the measured RMs are presented in Table 2. The QU-fits are shown in Supplementary Figure 3. The measured RMs have large uncertainties due to covariances between the fit parameters, which is difficult to alleviate due to the low number of rotations (due to either RM or delay) across the burst frequency extent. We conclude that the bursts in this work have consistent RM values (B2's RM is slightly over 3σ from B3, but this apparent difference should be verified in future observations of this source using an independent delay calibrator), which is also in agreement with the previously reported RM (−29.8 rad m^{-2}) [23]. We note that neither this work nor Bhardwaj et al. [23] correct for the ionospheric contribution to the RM, but this effect is likely to be $\lesssim 2$ rad m^{-2}.

The data for each burst were then corrected for the measured delay and RM. The polarization position angle (PPA) was calculated using the following equation:

$$\mathrm{PPA} = 0.5 \arctan\left(\frac{U}{Q}\right), \quad (9)$$

and, to correct for the parallactic angle, this is rotated by

$$\theta = 2\tan^{-1}\left(\frac{\sin(\mathrm{HA})\cos(\phi_{\mathrm{lat}})}{(\sin(\phi_{\mathrm{lat}})\cos(\delta) - \cos(\phi_{\mathrm{lat}})\sin(\delta)\cos(\mathrm{HA})}\right), \quad (10)$$

where HA is the hour angle of the burst, ϕ_{lat} is the latitude of the Effelsberg telescope, and δ is the declination of FRB 20200120E. Due to the fact that our observations did not feature an independent polarization calibrator scan, there remains an uncalibrated absolute phase offset in the data. Therefore, we cannot compare the PPAs between our two observational epochs, or with other PPA measurements of FRB 20200120E. By allowing for individual RM values per burst, we find that B1 and B2 exhibit a ΔPPA of 28.5°, and the ΔPPA between B3 and B4 is 21.7°. The unbiased linear polarization is computed following Everett & Weisberg [63], where

$$L_{\mathrm{unbias}} = \begin{cases} \sigma_I \sqrt{\left(\frac{L_{\mathrm{meas}}}{\sigma_I}\right)^2 - 1}, & \text{if } \frac{L_{\mathrm{meas}}}{\sigma_I} \geq 1.57 \\ 0, & \text{otherwise} \end{cases} \quad (11)$$

where $L_{\mathrm{meas}} = \sqrt{Q^2 + U^2}$, and σ_I is the standard deviation in the off-burst Stokes I data.

Bursts B1 – B4 are highly linearly polarized (> 90%), and exhibit little-to-no evidence for circular polarization. There is a tentative $3-4\,\sigma$ detection of 13 % and 6 % circular polarization in B2 and B4, respectively. The linear and circular fractions, as well as the PPA offset from a weighted mean PPA of bursts from a single epoch, are presented in Table 2, and the polarization profile and PPA for each burst is shown in Figure 2.

It has been seen in the literature that some repeating FRBs exhibit a constant PPA (Δ(PPA) < 10°) and RM per observing epoch [13,15]. Therefore, in addition to the individual burst RM measurements, we fit for a global RM per observing epoch. In this global fit, we find that the PPA of B1 and B2 differ by 68.3° (Table 2). This large ΔPPA may result from the low S/N of burst B1. The ΔPPA between B3 and B4 in this global fit is 23.6°, comparable to the difference we measured in the independent-RM fit above, unsurprising given the very similar RM values in the independent fits.

References

[80] Cordes, J. M. & McLaughlin, M. A. Searches for Fast Radio Transients. *Astrophys. J.* **596,** 1142–1154 (2003).

[81] Remazeilles, M., Dickinson, C., Banday, A. J., Bigot-Sazy, M. A. & Ghosh, T. An improved source-subtracted and destriped 408-MHz all-sky map. *Mon. Not. R. Astron. Soc.* **451,** 4311–4327 (2015).

[82] Reich, P. & Reich, W. Spectral index variations of the galactic radio continuum emission : evidence for a galactic wind. *Astron. Astrophys.* **196,** 211–226 (1988).

[83] Mather, J. C. *et al.* Measurement of the Cosmic Microwave Background Spectrum by the COBE FIRAS Instrument. *Astrophys. J.* **420,** 439 (1994).

[84] Rickett, B. J. Radio propagation through the turbulent interstellar plasma. *Annu. Rev. Astron. Astrophys.* **28,** 561–605 (1990).

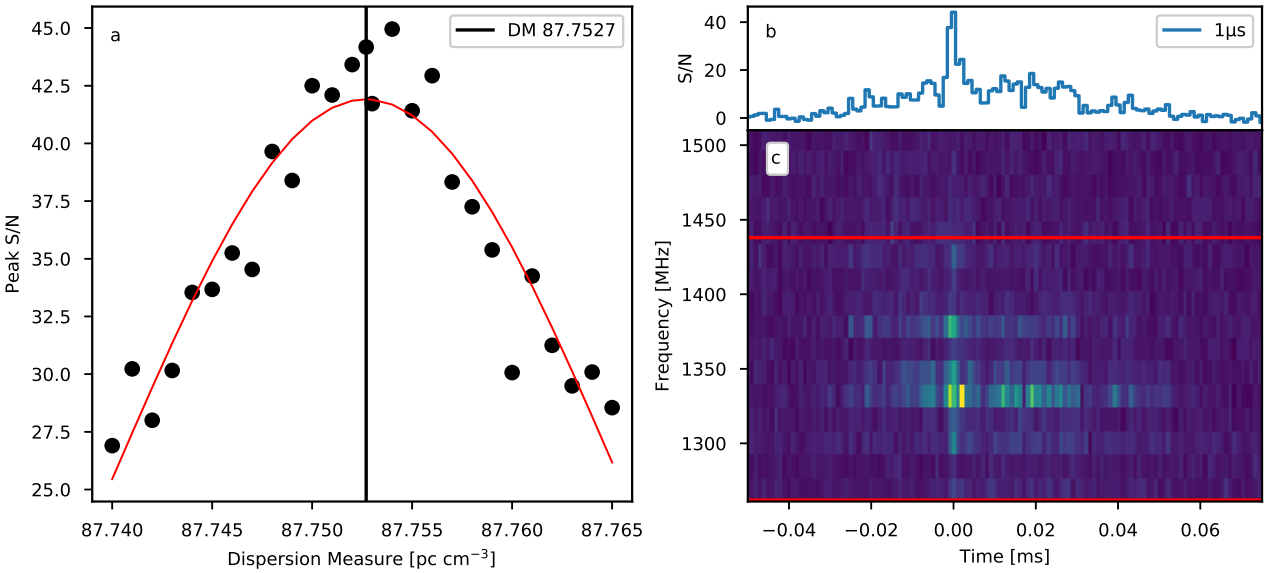

Supplementary Figure 1: Constraining the dispersion measure (DM) using the short timescale structure in burst B3 from FRB 20200120E. Using data products generated using SFXC[53], with a time and frequency resolution of 500 ns and 1 MHz, respectively, we coherently (within subbands) and incoherently (between subbands) dedisperse to a range of DMs, downsample in time by a factor of 2, and compute the peak S/N of the frequency-averaged profile (panel **a**). Also plotted in panel **a** is a Gaussian fit to the peak S/N as a function of DM, with the best-fit DM (DM = 87.7527±0.0003 pc cm^{-3}) shown by the grey line. Panel **b** shows the burst profile and panel **c** the dynamic spectrum coherently and incoherently dedispersed to the best-fit DM. The time and frequency resolutions used for plotting are 1 μs and 16 MHz, respectively. The red lines on the dynamic spectrum indicate the frequency extent averaged over to determine the peak S/N per DM, and to produce the burst profile.

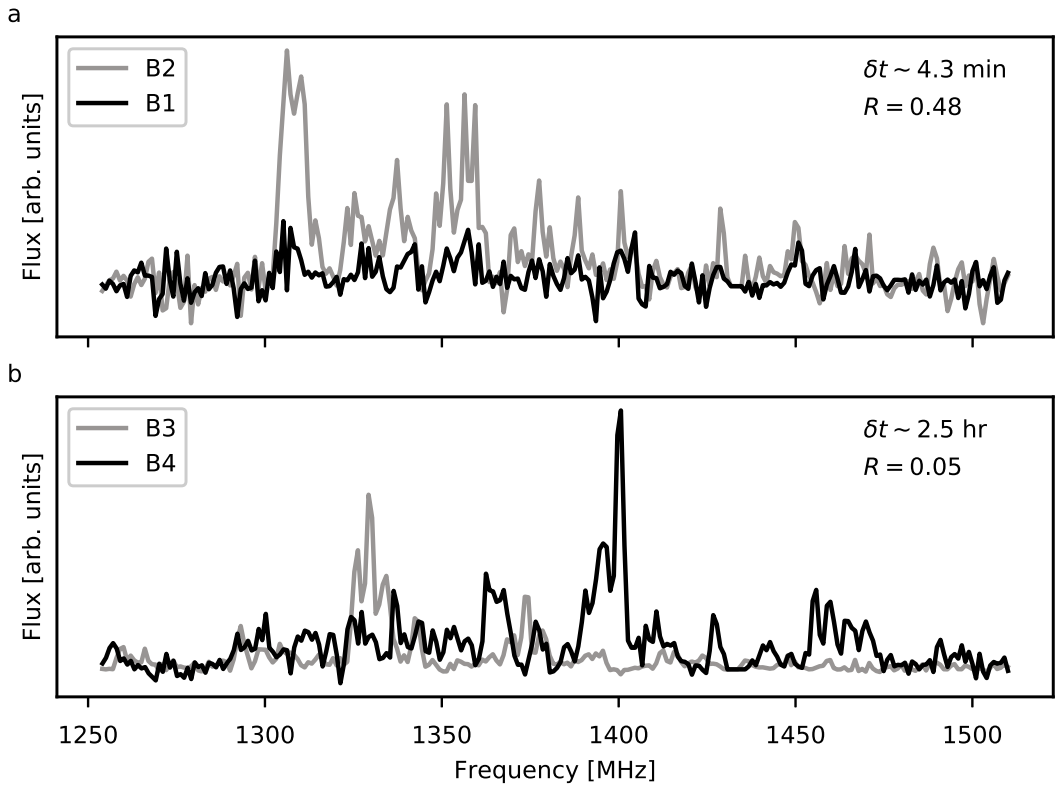

Supplementary Figure 2: Comparing the time-averaged spectra between bursts detected close in time. Panel **a** shows the time-averaged spectra for B1 (black) and B2 (grey). Panel **b** shows the time-averaged spectra for B3 (grey) and B4 (black). In the top right of each panel, we quote the time between the two bursts in the plot, δt, and the correlation coefficient of the burst spectra, R.

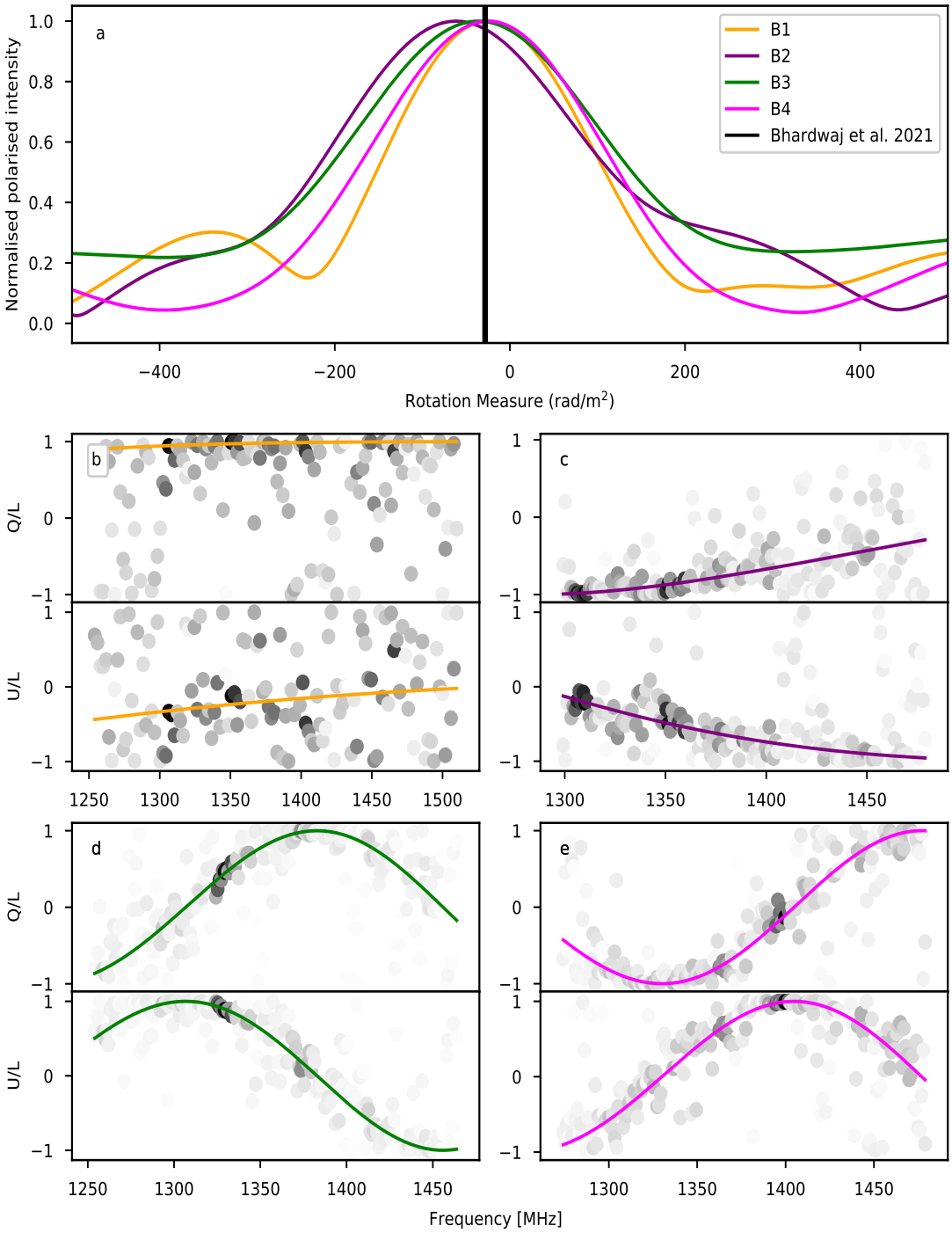

Supplementary Figure 3: Rotation measure (RM) determination for B1 – B4 from FRB 20200120E. Panel **a** shows the Faraday spectrum per burst (labelled), determined using RM synthesis[88], with the grey line showing the previous RM measurement of this source[23]. The grey-scale scatter points panels **b–e** show the Stokes Q (top) and Stokes U (bottom) spectra normalised by the linear polarization L= $\sqrt{Q^2 + U^2}$, where the darker color represents a higher S/N. The colored lines show the best-fit QU-fitting result, where we fit for both the RM and the delay between the polarization channels (Methods). The color of the line indicates which burst is being plotted, using the legend in the top figure.

Supplementary Table 1: High time resolution autocorrelation function and power spectra results.

Burst	Characteristic timescales [μs]	Red. χ^2 [a]	Power law index [b]	Δ Bayesian Information Criterion[c]	Goodness of fit p-value[d]	Outlier p-value[e]
B2	28.5 ± 0.2	2.0	1.85 ± 0.04	−20.5	0.50	0.98
B3	0.04 ± 0.3, 1.1 ±0.4, 35.6 ±0.5	2.4, 1.64, 1.3	1.46 ± 0.05	−12.1	0.53	0.99
B4	0.05 ± 0.02, 64.1 ± 1.5	2.7,1.9	2.04 ± 0.05	−15.4	0.66	0.97

[a] The reduced χ^2 of the Lorenzian fit to the high time resolution ACF in Extended Data Figures 4–6.
[b] The power law index measured for the power spectra.
[c] Metric for model comparison (BIC for power law red noise model − BIC for power law plus Lorentzian).
[d] Goodness of fit of the best fit model.
[e] p-value of the highest outlier in the residuals of the power spectrum.

[85] Cordes, J. M. & Lazio, T. J. Interstellar Scattering Effects on the Detection of Narrow-Band Signals. *Astrophys. J.* **376,** 123 (1991).

[86] van Straten, W., Manchester, R. N., Johnston, S. & Reynolds, J. E. PSRCHIVE and PSRFITS: Definition of the Stokes Parameters and Instrumental Basis Conventions. *Publ. Astron. Soc. Aust.* **27,** 104–119 (2010).

[87] Gould, D. M. & Lyne, A. G. Multifrequency polarimetry of 300 radio pulsars. *Mon. Not. R. Astron. Soc.* **301,** 235–260 (1998).

[88] Brentjens, M. A. & de Bruyn, A. G. Faraday rotation measure synthesis. *Astron. Astrophys.* **441,** 1217–1228 (2005).